



HAL
open science

The Hot Main Kuiper Belt Size Distribution from OSSOS

Jean-Marc C. Petit, Brett Gladman, J. Kavelaars, Michele Bannister, Mike
Alexandersen, Kathryn Volk, Ying-Tung Chen

► **To cite this version:**

Jean-Marc C. Petit, Brett Gladman, J. Kavelaars, Michele Bannister, Mike Alexandersen, et al.. The Hot Main Kuiper Belt Size Distribution from OSSOS. *The Astrophysical journal letters*, 2023, 947 (1), pp.L4. 10.3847/2041-8213/acc525 . hal-04194903

HAL Id: hal-04194903

<https://hal.science/hal-04194903>

Submitted on 4 Sep 2023

HAL is a multi-disciplinary open access archive for the deposit and dissemination of scientific research documents, whether they are published or not. The documents may come from teaching and research institutions in France or abroad, or from public or private research centers.

L'archive ouverte pluridisciplinaire **HAL**, est destinée au dépôt et à la diffusion de documents scientifiques de niveau recherche, publiés ou non, émanant des établissements d'enseignement et de recherche français ou étrangers, des laboratoires publics ou privés.

1
2 CC-BY 4.0 (<https://creativecommons.org/licenses/by/4.0/>)

DRAFT VERSION MARCH 17, 2023

Typeset using L^AT_EX **manuscript** style in AASTeX631

The hot main Kuiper belt size distribution from OSSOS

3 JEAN-MARC PETIT ¹, BRETT GLADMAN ², J. J. KAVELAARS ^{3,4,2}, MICHELE T. BANNISTER ⁵,
4 MIKE ALEXANDERSEN ⁶, KATHRYN VOLK ^{7,8} AND YING-TUNG CHEN ⁹

5 ¹*Institut UTINAM UMR6213, CNRS, OSU Theta F25000 Besançon, France*

6 ²*Department of Physics and Astronomy, University of British Columbia, 6224 Agricultural Road, Vancouver, BC V6T*
7 *1Z1, Canada*

8 ³*Herzberg Astronomy and Astrophysics Research Centre, National Research Council of Canada, 5071 West Saanich*
9 *Rd, Victoria, British Columbia V9E 2E7, Canada*

10 ⁴*Department of Physics and Astronomy, University of Victoria, Elliott Building, 3800 Finnerty Rd, Victoria, BC*
11 *V8P 5C2, Canada*

12 ⁵*School of Physical and Chemical Sciences — Te Kura Matū, University of Canterbury, Private Bag 4800,*
13 *Christchurch 8140, New Zealand*

14 ⁶*Center for Astrophysics | Harvard & Smithsonian, 60 Garden Street, Cambridge, MA 02138, USA*

15 ⁷*Lunar and Planetary Laboratory, The University of Arizona, 1629 E University Blvd, Tucson, AZ 85721, USA*

16 ⁸*Planetary Science Institute, 11700 East Fort Lowell, Suite 106, Tucson, AZ 85719, USA*

17 ⁹*Institute of Astronomy and Astrophysics, Academia Sinica, No. 1, Sec. 4, Roosevelt Rd., Taipei 10617, Taiwan*

18 (Received March 17, 2023; Revised; Accepted)

19 Submitted to PSJ or ApJ Letters???

20 ABSTRACT

21 Using the absolute detection calibration and abundant detections of the OSSOS
22 (Outer Solar System Origin Survey) project, we provide population measurements for

Corresponding author: Jean-Marc Petit
Jean-Marc.Petit@normalesup.org

the main Kuiper Belt. For absolute magnitude $H_r < 8.3$, there are 30,000 non-resonant main-belt objects, with twice as many hot-component objects than cold, and with total mass of $0.014 M_\oplus$, only 1/7 of which is in the cold belt (assuming a cold-object albedo about half that of hot component objects). We show that transneptunian objects with $5.5 < H_r < 8.3$ (rough diameters 400–100 km) have indistinguishable absolute magnitude (size) distributions, regardless of being in the cold classical Kuiper belt (thought to be primordial) or the ‘hot’ population (believed to be implanted after having been formed elsewhere). We discuss how this result was not apparent in previous examinations of the size distribution due to the complications of fitting assumed power-law functional forms to the detections at differing depths. This shared size distribution is surprising in light of the common paradigm that the hot population planetesimals formed in a higher density environment much closer to the Sun, in an environment that also (probably later) formed larger (dwarf planet and bigger) objects. If this paradigm is correct, our result implies that planetesimal formation was relatively insensitive to the local disk conditions and that the subsequent planet-building process in the hot population did not modify the shape of the planetesimal size distribution in this 50–300 km range.

1. INTRODUCTION

The size distribution of objects produced at various stages of the planet formation process is a topic of intense interest (eg. [Kenyon 2002](#); [Kobayashi et al. 2016](#); [Ormel 2017](#); [Schaller & Brown 2007](#); [Schlichting & Sari 2011](#); [Shannon et al. 2016](#)). One must conceptually separate the size distribution of objects directly built by some planetesimal formation process from those that are then created by either collisional grinding or accumulation ([Kenyon et al. 2008](#); [Morbidelli & Nesvorný 2020](#)). In the main asteroid belt there has been heavy collisional modification which has greatly obscured the initial size distribution, although arguments that many asteroids were ‘born big’ have been made ([Johansen et al. 2007](#); [Morbidelli et al. 2009](#)). The non-saturated cratering record on Pluto/Charon and Arrokoth

(Greenstreet et al. 2019; Singer et al. 2019; Spencer et al. 2020) argues that in the transneptunian region the size distribution has not been modified by collisional and accretional effects since the surfaces of these bodies formed. If true this would mean that the currently essentially collisionless environment of the Kuiper Belt (Abedin et al. 2021; Greenstreet et al. 2019; McKinnon et al. 2020; Petit & Mousis 2004) has persisted for the Solar System’s age and that the size distributions are thus primordial and preserve the outcome of the planetesimal formation and planet building process.

The recent study of Kavelaars et al. (2021) used an ensemble of survey samples (Kavelaars et al. 2009; Petit et al. 2011; Alexandersen et al. 2016; Petit et al. 2017; Bannister et al. 2018), referred to collectively as OSSOS++, to show that the dynamically cold classical Kuiper belt’s size distribution follows a power-law with an exponential cutoff at the large size end. This ‘exponential taper’ shape is compatible with the initial mass function obtained in simulations of planetesimal formation in a streaming instability scenario (Schäfer et al. 2017; Li et al. 2019) and while other low-density formation scenarios exist (eg. Shannon et al. 2016), which mechanism created planetesimals is irrelevant for this present manuscript. Several independent facts (Petit & Mousis 2004; Parker & Kavelaars 2010; Tegler et al. 2003; Pike et al. 2017; Schwamb et al. 2019; Greenstreet et al. 2019; Abedin et al. 2021; McKinnon et al. 2020) also hint at an *in-situ* formation of the cold belt in a low density environment.

The region where the cold belt resides, between the 3:2 and 2:1 mean motion resonance with Neptune, also contains resonant Trans-Neptunian Objects (TNOs) and other non-resonant, yet excited TNOs (objects with either large eccentricity e or inclination i , or both) forming the hot belt. These objects are commonly stated to have been formed in a region closer to the Sun and then implanted in the Kuiper belt during late planetary migration, based on dynamical (reviewed by Nesvorný 2018) and compositional (Schwamb et al. 2019) arguments. The goal of this manuscript is to use the OSSOS++ sample and compare the absolute magnitude distribution of the hot belt to that of the cold belt; we find that the two distributions are extremely similar over the magnitude range where we have high accuracy.

In the next section, we present the OSSOS++ sample of hot objects and compare its size distribution to that of the cold population. We extend the OSSOS++ sample with the MPC database to the large size side of the distribution. Next we present some cosmogonic implications of our findings.

2. THE OSSOS++ HOT POPULATION ABSOLUTE MAGNITUDE DISTRIBUTION

We use the OSSOS++ sample (see [Bannister et al. 2018](#), for full details) to determine the absolute magnitude distribution of the populations of the main classical Kuiper belt. The main-belt classicals are made up of the non-resonant, non-scattering objects with semimajor axes $39.4 \text{ au} < a < 47.7 \text{ au}$ (that is, between the 3:2 and 2:1 resonances, rejecting all resonant objects in this range).

As explained in [Van Laerhoven et al. \(2019\)](#) and [Kavelaars et al. \(2021\)](#), the best single parameter to discriminate between the cold and the hot populations of the main classical Kuiper belt is the free inclination with respect to the a -dependent Laplace plane. [Huang et al. \(2022a\)](#) provide an improved determination of the local Laplace plane by double-averaging over the two fast angles rather than from the classical first order secular theory; the resulting free inclinations are very stable over time and can be found¹ in [Huang et al. \(2022b\)](#). Given the distribution of the free inclinations shown in Fig. 3 of [Huang et al. \(2022a\)](#), in our manuscript we elect to use $i_{free} < 4.5^\circ$ as an acceptable split between the main-belt cold and hot populations (understanding there will be interlopers at some level). The *cold* classical belt only exists at $a > 42.4 \text{ au}$ ([Kavelaars et al. 2008](#)), and is heavily concentrated to perihelia $q > 39 \text{ au}$ ([Petit et al. 2011](#)) and (see Fig. 5 of [Gladman & Volk 2021](#)). We here adopt these simple cuts to define the cold classical belt region, arguing that the higher eccentricities for TNOs with $q < 39 \text{ au}$ and $a > 42.4 \text{ au}$ indicate they have suffered dynamical excitation. The *hot* main-belt population is then all objects not in the cold sample. This yields 327 cold and 219 hot objects in OSSOS++.

2.1. Sample characterization

¹ The main-belt free inclinations can also be found at <http://yukunhuang.com>.

97 We use the method in [Kavelaars et al. \(2021\)](#) to debias the orbit and H_r distributions of the
 98 OSSOS++ detections². The most difficult TNO orbits to detect, at a given H_r , are those with
 99 near-circular orbits at the $a \simeq 47$ au outer edge of the main belt. Objects on such orbits always
 100 remain at distance $d \simeq 47$ au, while those with either lower a or larger eccentricity e will spend
 101 some time closer to the Sun and be visible for some fraction³ of their orbital longitude. Because
 102 OSSOS++ reached apparent magnitude $m_r \gtrsim 25$ for some blocks, $H_r \simeq 8.3$ TNOs are visible at
 103 47 au; [Kavelaars et al. \(2021\)](#) used this H_r for the limit down to which we trust our debiasing for the
 104 cold population; even if the higher e 's of hot TNOs give a mild increase in sensitivity to $H_r > 8.3$
 105 hot-object orbits, we maintain the limit at 8.3 since our goal is to compare the two populations as a
 106 function of absolute magnitude. Because this debiasing method uses only the detections, this model
 107 will certainly increasingly underestimate TNO numbers beyond these sensitivity limits.

108 Simple binned histograms to represent a differential distribution are subject to large fluctuations
 109 when the sample is not very numerous. To avoid this shortcoming, we use a Kernel Density Estimator
 110 (KDE) method which spreads out each detection over a kernel of some size; each detection thus
 111 contributes to the differential distribution not only at its exact position but on some interval with a
 112 varying weight (see appendix A). Figure 1 presents these debiased differential TNO numbers (per 0.25
 113 magnitudes, in order to compare with the known sample in the Minor Planet Center, MPC) as the
 114 hot and cold populations implied by the OSSOS++ detections. MPC H magnitudes are converted
 115 to $H_r = H_{MPC} - 0.2$; this is the known shift between OSSOS++ H_r magnitudes and the H stated
 116 in the MPC. The rollover in the cold distribution for $H_r > 8.3$ where we expected to insensitivity to
 117 begin is clear; the rollover in the hot distribution begins a few tenths of a magnitude fainter due to
 118 the ability to detect the lower perihelion objects present in that population (as mentioned above).

² Divide the phase space in small $(a, q, \sin(i), H)$ cells; for any cell with a detection in it, determine the detection bias of this cell using the Survey Simulator.

³ Using $H_r = 9.0$ as an example, $a = 47$ au circular orbits can never be observed by OSSOS, while $H_r = 9$ objects distributed along an $e \simeq 0.1$ orbit rise above the flux threshold close to perihelion and give one sensitivity to that set of a, q orbital elements for the purposes of debiasing (where debiasing is essentially taking into account Kepler's Second Law). The method has no ability, however, to debias the orbit for which there is never any possibility of detection.

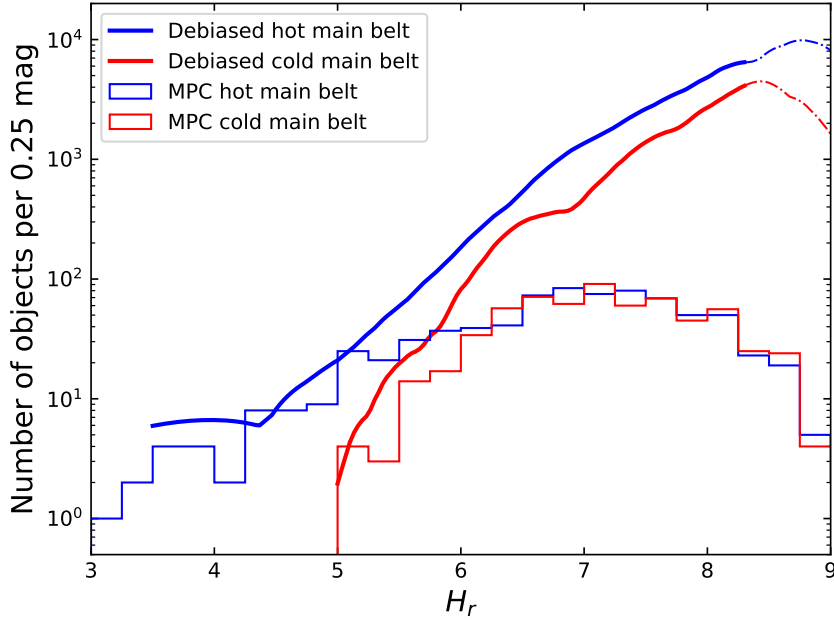


Figure 1. Calibrated differential H_r distribution of the main-belt hot (blue bold curve) and cold (bold red curve) components from debiasing the OSSOS++ sample for $H_r \in [3; 8.3]$. Less secure estimates (see text) for $8.3 < H_r < 9$, which are only lower limits, are shown by dash-dotted curves. These curves are Epanechnikov Kernel Density Estimates (appendix A) of the debiased H_r absolute magnitude distributions of the main classical belt objects in OSSOS++. The dotted lines represent 95% confidence intervals from Poisson statistics. Up to $H_r \simeq 5.3$ the OSSOS absolute calibration reproduces the MPC numbers, indicating the latter is now essentially complete in the main-belt.

119 Several important results follow immediately from Fig. 1. First, the MPC inventory (shown as
 120 histograms) of the main belt is very close to complete for $H_r < 5.3$; this was already clear for cold
 121 TNOs (Kavelaars et al. 2021) but our estimates reinforce the idea that the hot *main-belt population* is
 122 also now essentially complete. Sheppard et al. (2011) already suggested that the TNO inventory was
 123 nearly complete to apparent magnitude $M_R \simeq 21$, corresponding to $H_r \simeq 6.4$ at 30 au and $H_r \simeq 4.2$ at
 124 50 au. Despite a burst of $H_r < 5.3$ discoveries during 2013-2015 by Pan-STARRS (Weryk et al. 2016)
 125 no bright main-belt TNOs have been discovered despite continued operations, signifying completeness
 126 to this magnitude. The agreement of our estimates with the complete population at the bright end
 127 shows that our debiasing method yields correct number estimates; these estimates then establish

128 that $H_r > 5.8$ is largely incomplete (the known TNOs are below our 95% confidence intervals). The
 129 up-coming LSST will survey the main classical Kuiper belt down to $H_r \simeq 7.5$ at 47 au; Figure 1
 130 indicates that LSST will mostly discover TNOs at H magnitudes for which completeness in 2022 is
 131 still only $\simeq 5\%$. Secondly, one is struck that the hot and cold populations have rather similar H_r
 132 distribution shape in the range [5.8, 8.3]. This is surprising because many papers (Bernstein et al.
 133 2004; Elliot et al. 2005; Petit et al. 2011; Adams et al. 2014; Fraser et al. 2014) conclude that the hot
 134 and cold components have different absolute magnitude distributions. Here we suggest that these
 135 differences might be dominantly confined only to the largest ($H_r < 6$) TNOs of the populations; if
 136 true, this has major implications for the planetesimal formation and planet-building process.

137 2.2. Comparison of the hot and cold distributions

138 Figure 2 shows a clearer representation of the shape similarity of the two populations. Note that OS-
 139 SOS++ has a sufficiently large number of detections that construction of a differential H -magnitude
 140 and good resolution is possible; many past analyses have shown cumulative distributions. Here, we
 141 have multiplied the number of cold TNOs by a factor of 2.2, which matches the curves at $H_r = 6$.
 142 Given the uncertainties shown by the 95% confidence ranges and the expectation to have a small part
 143 of this range at $\simeq 2\sigma$ discrepancy, the shapes are nearly identical in the range from $5.5 < H_r < 8.3$,
 144 with the most compelling indication of a difference at $H_r < 6$ where the exponential taper cuts off
 145 the cold population. For $H_r < 5$, Fig. 1 makes it clear that the hot population contains large objects
 146 while the cold belt has none.

147 A χ^2 test can quantitatively evaluate if one can reject the null hypothesis that the two observed
 148 distributions are drawn from the same underlying distribution in the range from $\simeq 5.5$ –8.3. In order
 149 to mitigate binning effects, we varied differential bin sizes (0.2, 0.3, or 0.4 mag) and the histogram
 150 starting magnitude (by steps of 0.1 mag), yielding probabilities that the two distributions are from the
 151 same underlying distribution ranging from 55% to 90%; the idea that the distributions are identical is
 152 clearly plausible. Fig. 2 also shows the exponential taper function derived in Kavelaars et al. (2021);
 153 another χ^2 test to compare the hot H_r distribution to that function (only shifting the function to

154 match the debiased hot number at the single value of $H_r = 8.0$) yields probabilities between 50% and
 155 80% of drawing the hot population from the same functional form as the cold in this same H_r range.

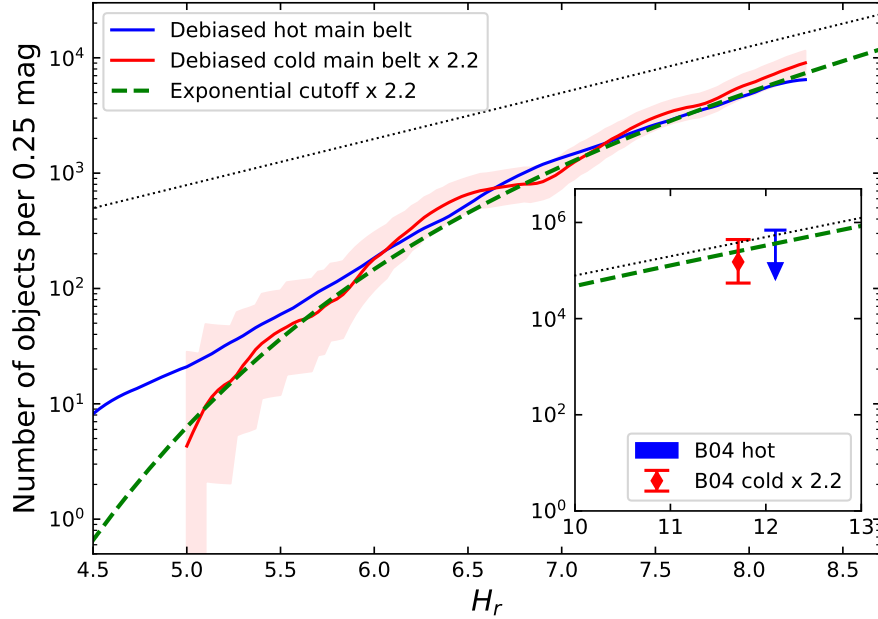


Figure 2. Similar to Fig. 1, where here the debiased cold component estimates and uncertainties have been scaled upward by a factor of 2.2. The green dashed line shows the [Kavelaars et al. \(2021\)](#) cold population exponential cutoff fit (with large- H asymptotic slope of 0.4), also scaled upward by a factor of 2.2. The inset shows the continuation of the scaled exponential cutoff fit at larger/fainter H_r ; the red error-bar gives the 95% confidence range from the detection of three cold TNOs using HST by [Bernstein et al. \(2004\)](#), and is compatible with the above extrapolation. The inset’s blue arrow shows the 95% confidence upper limit from the non-detection of hot population TNOs in that same HST study. For $H_r > 5.5$ the shape of the hot and cold population’s are surprisingly similar, which hints at similar formation processes. The black dotted line is a reference exponential with logarithmic slope $\alpha = 0.4$, to help see how the exponential taper deviates from a single exponential.

156 [Kavelaars et al. \(2021\)](#) showed that if one extends the H_r -distribution beyond 8.3 with a functional
 157 form asymptotic to an exponential law $dN/dH \propto 10^{0.4H}$, the resulting estimated differential numbers
 158 are consistent with the detection of three $H_r < 12$ cold TNOs in the HST search of [Bernstein et al.](#)
 159 (2004). A similar extrapolation of our hot main-belt population estimate is consistent with no hot

160 detections in the HST search.⁴ An asymptotic power of $0.4H_r$ is supported for $H_r \simeq 12 - 17$ by
 161 the crater record on Charon (Singer et al. 2019), which has been estimated to be dominated by hot
 162 population projectiles (Greenstreet et al. 2015).

163 Thus, there is as yet no firm evidence that the shape of the H magnitude distributions of the
 164 hot and cold are different for $H_r \gtrsim 5.5$. But if the cold classical belt is formed in situ in a low-
 165 density environment (exhibiting an exponential cutoff at a size scale set by local conditions at \simeq
 166 44 au) and the hot object implanted after being formed much closer to the Sun (having a different
 167 formation, collision, and dynamical history), one might reasonably expect them to have very different
 168 H magnitude distributions. We will return to this issue in the discussion section after discussing the
 169 small- H regime, where the two populations differ markedly.

170 2.3. *The large size tail*

171 The sample of large bodies from the main classical Kuiper belt in the MPC database is very close
 172 to complete for the cold (Kavelaars et al. 2021, and Figure 1) and the hot (Figure 1) populations
 173 down to $H_r \simeq 5.3$. Hence the H_r distribution at large sizes can be directly obtained from the MPC
 174 database. The debiased OSSOS++ sample fails to explore the $H_r < 4$ range due to limited sky area
 175 covered and the resulting tiny number of detections (only one hot main-belt object brighter than
 176 $H_r = 5$ and three with $H_r < 5.5$).

177 Figure 3 shows the cumulative number of objects present in the MPC database for hot main classical
 178 belt (blue line) and all hot (black line) objects. It is noteworthy that the full hot sample, although
 179 obviously incomplete (because even the largest objects cannot be seen at the large distances reached
 180 by the scattering and resonant populations), is parallel to the hot main-belt sample, which is complete
 181 bright-ward of $H_r \simeq 5.3$. The abrupt change at $H_r \simeq 3.3$ in both distributions has been evident
 182 (Brown 2008) since large shallow surveys first covered most of the sky and continues to signal an

⁴ Despite the hot population having a factor of two more TNOs than the cold population at each $H_r > 5.8$ magnitude, non-detection in the HST survey is understood when one considers that these hot objects are spread out over an order of magnitude more sky area due to their larger orbital inclinations.

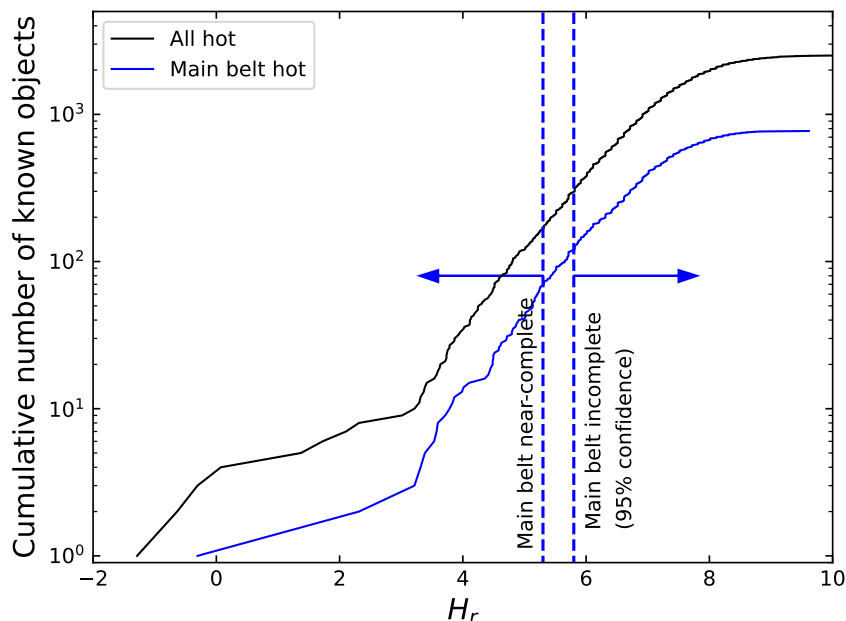


Figure 3. Cumulative H_r distribution (black curve) of all hot TNOs (here, $a > 29.5$ au and not in the cold population) in the MPC database as of 13 January 2022. The blue curve shows the main-belt subset. The vertical line at $H_r = 5.3$ represents where our analysis indicates that the the hot main-belt population is nearly complete. The vertical line at $H_r = 5.8$ shows where the MPC sample is certainly incomplete (95% confidence level). The two samples share very similar H_r distributions brighter than $H_r = 5.3$ (in particular both distributions show an obviously shallower slope for $H_r < 3$), supporting the claim that all hot objects have the same origin.

183 abrupt change of exponential index between 0.14 and 0.6 at this magnitude (Ashton et al. 2021). We
 184 will refer to the $H_r < 3.3$ range as the ‘dwarf planet’ regime⁵ below.

185 Fortuitously, the bright end of OSSOS++ happens to lie at the hot main-belt completeness limit.
 186 The argument above indicates we can graft our debiased hot distribution onto the MPC sample
 187 and, with the parallel distribution the full hot sample allows one to have access to the H_r -magnitude
 188 distribution from Pluto/Eris scale down to $H_r = 8.3$ (and further by reasonable extension to the HST

⁵ Although the current IAU dwarf planet definition involves difficult to know properties related to ‘roundness’ (e.g. Tancredi & Favre 2008; Grundy et al. 2019), we point out that using a simple $H_V < 3.5$ definition would make the terminology adapt to some obvious transition in the object distribution.

study's depth at $H \simeq 12$). The hot-cold comparison indicates that consistency of the H_r -magnitude shape for $H_r \gtrsim 5.5$ is not also true at bright absolute magnitudes. The cold population exhibits the exponential cutoff while the hot population (both in the main belt and in general) not only lacks the exponential cutoff but has very shallow distribution as one goes up in size into the dwarf planet regime. We will interpret this in the Discussion section below.

3. CONSIDERATION ON PAST SURVEYS

Because of the curved shape of the exponential cutoff, representing the H -distribution by a single exponential $N(< H_r) \propto 10^{\alpha H_r}$ yields different logarithmic slopes α depending on the area and depth of the survey. A shallow, wide survey will probe the steep part of the curve, while a fainter, narrower survey will probe a shallower part of the curve. The case of the hot component is even worse, due to the change between the logarithmic slopes of ~ 0.6 in the range $H \in [3.5; 6]$ and 0.14 for brighter objects (Ashton et al. 2021). A single exponential representation will thus require a very shallow slope for wide, shallow survey, to medium steep for intermediate surveys, and then again again shallow slopes for fainter surveys. Many of the early works did not separate between the hot and cold populations. Surveys close to the ecliptic were dominated by the cold component, while surveys mostly out of the ecliptic missed much or all of the cold population. To blur things even more, these studies used the apparent magnitude, thus convolving the H -distribution with the distance distribution (see Petit et al. 2008, for a review).

More recent studies directly determined the H distribution, using either a single exponential when the range of H magnitudes is small (e.g. Petit et al. 2011; Adams et al. 2014) or a double exponential when the range of H magnitudes was large (Fraser et al. 2014). Petit et al. (2011) separately modeled the cold and hot components to their limit of $H_r \lesssim 7.5$ and obtained different size distributions for the two components, with population measurements to that H -magnitude limit. The number of $D > 100$ km TNOs in the hot and cold main belt given in Petit et al. (2011) were extrapolations with these single slopes (0.8 for hot and 1.2 for cold), beyond the range where they were measured. It is now clear that these slopes do not represent the H -magnitude distribution beyond 7.5 (which flattens steadily) and thus the extrapolation overestimated the $D > 100$ km populations, likely

more so for the cold population than for the hot one. When including small (faint) TNO surveys, Fraser et al. (2014) used a double exponential with breaks around $H_r=7-8$ where the bright part was essentially the same single exponentials for the two components as Petit et al. (2011).

The sparseness of data from homogeneous characterized surveys and the use of particular functional forms prevented the recognition of the similarity of the hot and cold size distributions in the few 10s km to ~ 300 km range.

4. POPULATION AND MASS ESTIMATES

Using our derived H_r distribution, we can provide an accurate debiased main-belt population (which does not include resonant or scattering TNOs) as a function of H_r and also number and mass estimates (which are more uncertain) for TNOs larger than a certain diameter.

4.1. Population estimates

Table 1 gives estimated TNO numbers at the faintest absolute magnitude we confidently debias ($H_r \leq 8.3$) and for H_r values corresponding to a diameter $D=100$ km for various commonly-used values of the albedo (eq. B2). We added a column with $\nu_r = 0.24$, the albedo of Arrokoth determined by Hofgartner et al. (2021) in r band filter. Note that here all estimates are based on direct debiasing, which is very uncertain for $H_r = 8.9$. Alternately, to estimate numbers of $H_r < 8.9$ TNOs, one could use the exponential cutoff formula (eq. B4) for the cold population and multiply by 2.2 for the hot population; Table 1's last column would then read 21, 47, and 68 thousand TNOs, which is identical given the uncertainties. This is consistent with our previous work at the older measurement limit: Petit et al. (2011, Table 5) estimated $N(H_g < 8.0) = (8 \pm 2) \times 10^3$, in agreement with our current $N(H_r < 7.3) = 6.7_{-1.6}^{+1.3} \times 10^3$ if one uses an averaged $g - r \simeq 0.7$ color.

Our debiasing gives an estimate of the total population of main-belt classical TNOs which we can compare to other well sampled small-body populations. Out of curiosity, we note that the main classical Kuiper belt contains 340 and 31,000 objects brighter than $H_r = 6.0$ and 8.3 respectively, while there are only 10 and 145 Main Belt Asteroids (MBAs) brighter than those magnitudes. Comparison with the jovian Trojan population has more cosmogonic interest because the hot classicals and

Table 1. OSSOS++ population estimates from direct debiasing for main-belt non-resonant TNOs (in 10^3 objects). Population estimates marked with a * are likely underestimates (Sec. 2.1) because $D = 100$ km corresponds to $H_r > 8.3$ for $\nu_r = 0.04$. The 2 left(right) columns in $D \geq 100$ km part mostly cover the sample mean for the cold (hot) populations (respectively); although the literature gives different average albedos for the hot and cold populations, the uncertainty on individual measurements, possible systematics due to modeling, and the sample scatter means that individual object albedos could always cover the whole range, resulting in order of magnitude uncertainty in population estimates larger than D . In contrast, the $H_r < 8.3$ estimates are much more precise.

component	$H_r \leq 8.3$	$D \geq 100$ km			
		$\nu_r = 0.24$ ($H_r \leq 7.1$)	$\nu_r = 0.15$ ($H_r \leq 7.5$)	$\nu_r = 0.08$ ($H_r \leq 8.2$)	$\nu_r = 0.04$ ($H_r \leq 8.9$)
Cold	11 ± 1	1.2 ± 0.3	2.8 ± 0.5	9 ± 1	* 20 ± 2
Hot	20 ± 3	2.4 ± 0.7	7 ± 1	18 ± 3	* 46 ± 7
All	31 ± 4	3.6 ± 1	10 ± 2	27 ± 4	* 66 ± 9

242 other excited TNOs have been suggested to come from the same primordial population as the jovian
 243 Trojans (Morbideilli et al. 2005). In the $H_r=7.3-8.3$ range, our debiasing shows that the jovian Tro-
 244 jans have a similar H_r distribution to the hot TNO population, with the MPC Trojan sample being
 245 complete in that range (see Hender & Malhotra 2020, for completeness limits). There are 8 Jupiter
 246 Trojans with $H_r \leq 8.3$, and 20,000 hot main classical TNOs, thus implantation models of jovian
 247 Trojans and hot main classical TNOs must account for an efficiency ratio of order 3×10^3 . Nesvorný
 248 & Vokrouhlický (2016) and Nesvorný et al. (2016) state implantation efficiencies of $(7 \pm 3) \times 10^{-4}$ and
 249 $(7.0 \pm 0.7) \times 10^{-7}$ respectively for hot classicals and jovian Trojans; this model-based factor of 1000
 250 (with an uncertainty of at least a factor of 2) is thus similar to the observed factor of 3000. With
 251 OSSOS++, the $H_r < 8.3$ hot main-belt population is now the least fractionally uncertain number in
 252 this chain of reasoning but, as Table 1 shows, an order of magnitude population uncertainty appears
 253 due to the albedo uncertainty.

254 Using the CFEPS population estimates (Petit et al. 2011; Gladman et al. 2012) extrapolated to
 255 100 km size, Greenstreet et al. (2015, 2019) and Abedin et al. (2021) determined the expected number

of craters on the surface of Pluto, Charon, and Arrokoth formed in the last 4 Gyr of bombardment. They extrapolated the 100 km population down to kilometer-size projectiles using an exponential of slope $\alpha = 0.4$, concluding that the recorded crater numbers could be produced without a contribution of an early phase (see below) and that the dominant source of craters on Arrokoth is from cold population projectiles.

Our current estimates, however, indicate fewer 100 km bodies than the CFEPS extrapolation down to this size, by a factor of 3–30 depending on which albedo is used, which determines H for 100-km bodies.)⁶ Starting from $H \sim 6$ down to the limit of our survey, we find that that the hot population is 2.2 times larger than the cold. For smaller sizes (larger H), we *assume* that the exponential cutoff continues, thus the hot population remains twice the cold at any given H_r . Eq. (B4) then yields similar numbers of projectiles at $H_r \sim 17$ as found by Greenstreet et al. (2015, 2019) and Abedin et al. (2021), with now twice as many main-belt hot TNOs as cold, while before the extrapolation produced 2 to 3 times as many cold objects as hot due to the incorrect continuation of a very steep slope for cold objects to $H_g=8$. The ratio hot-to-cold could be even larger at a specific size (km) when one accounts for the possibly larger albedo for cold objects ($\nu_r \sim 0.15$) than for hot objects ($\nu_r \sim 0.08$). Remember that all this is an assumption, not directly based on observational evidence, and should be taken with a pinch of salt.

Thus all workers should now re-evaluate the Arrokoth cratering rate. Pluto and Charon will continue to be dominated by hot-population projectiles, while Arrokoth may cease to be dominated by cold-population impactors. Morbidelli et al. (2021) concluded dominance of the hot population for Arrokoth crater formation, but their numbers of 100 km and 2 km projectiles are not in line with our current estimates and should be re-visited.

4.2. Mass estimates

⁶ Petit et al. (2011) used an albedo $\nu_g = 0.05$ which means $\nu_r \sim 0.08$ for cold objects (assuming $\langle g - r \rangle \sim 0.9$) and $\nu_r \sim 0.06$ for hot objects (for $\langle g - r \rangle \sim 0.6$). If one instead uses $\nu_r = 0.15$ for cold and $\nu_r = 0.08$ for hot (see Appendix B), this means a brighter H_r magnitude for 100 km, again decreasing again the number of objects at that size.

279 In appendix B, we estimate the main-belt mass between the 3:2 and 2:1 mean-motion resonances,
 280 integrated over *all* sizes. We use bulk density $\rho = 1000 \text{ kg/m}^3$ and albedos $\nu_{r,c} = 0.15$ and $\nu_{r,h} = 0.08$
 281 for cold and hot TNOs, respectively (Fraser et al. 2014; Lacerda et al. 2014)⁷, except for objects
 282 larger than $\sim 500 \text{ km}$, where both density and albedo are known to increase (see Appendices B.1 and
 283 B.2.

284 Understanding that masses are uncertain to a factor of 3 due to poorly-constrained albedos and
 285 densities, we find a cold-belt mass of $0.002 M_{\oplus}$ for an exponential cutoff shape of H_r and $0.012 M_{\oplus}$
 286 for the hot belt, for a total mass of the main classical belt of $0.014 M_{\oplus}$. We find the same hot-belt
 287 mass as Fraser et al. (2014), but a cold-belt mass that is 7 times larger. Gladman et al. (2001)
 288 estimated a total mass for the 30–50 au distance range of $0.04\text{--}0.1 M_{\oplus}$, using an albedo $\nu_r = 0.04$ for
 289 all TNOs; this includes all dynamical components, but because the main belt represents only about
 290 half the mass (determined using the CFEPS model, Petit et al. 2011) in the 30–50 au distance range,
 291 a $0.02\text{--}0.05 M_{\oplus}$ estimate results. Using this 4% albedo, our current approach gives a slightly higher
 292 total classical main-belt mass $0.06 M_{\oplus}$.

293 Based on creation of a planetary ephemeris, Di Ruscio et al. (2020) estimated the total Kuiper Belt
 294 mass to be $(0.061 \pm 0.001)M_{\oplus}$, with unknown model-based uncertainty. This is $\simeq 4$ times higher than
 295 our estimate of the classical belt, but again only half of this $0.06M_{\oplus}$ would be main-belt TNOs. With
 296 the same method, but using a slightly different dataset, Pitjeva & Pitjev (2018) estimated the mass
 297 to be $(0.02 \pm 0.004)M_{\oplus}$, which when restricted to the main belt is in agreement with our estimate.

298 Because the tapered exponential lacks an abrupt break between a steep slope power-law (steeper
 299 than $\alpha = 0.6$ for H_r distribution or than $q = 4$ for D distribution⁸) to a shallow slope for small sizes,
 300 there is less of a concentration of mass to the typical diameter scale where the break occurs. For
 301 our estimated hot belt, the 25th and 75th percentile for mass are $H_r < 6.7$ and $H_r < 9.8$. For the
 302 cold population, the 25th percentile is $H_r < 7.3$ and the 75th percentile is at $H_r < 10.1$. Broadly

⁷ Note that Vilenius et al. (2014) reported very similar values of $\nu_{v,c} \sim 0.14$ and $\nu_{v,h} \sim 0.085$ in band v from Herschel and Spitzer observations.

⁸ The relations $N(< H) \propto 10^{\alpha H}$ and $dN/dD(D) = n(D) \propto D^{-q}$ are related by $q = 5\alpha + 1$ for a fixed albedo ν .

speaking, our precise knowledge of the size distribution includes an H magnitude range that contains about half the mass of the classical Kuiper belt.

Note that because of the very shallow $\alpha = 0.14$ (Ashton et al. 2021) in the $H_r < 3.5$ hot-object tail, it is possible that the largest TNOs in this tail were planetary scale and contained most of the mass of the hot-population formation region. These very massive objects have not been retained the hot main-belt or the hot population in general due to the $\sim 10^{-3}$ retention efficiency of the scattering out process Nesvorný & Vokrouhlický (2016), and thus one should remember that much of mass in the hot-formation region may have been sequestered into very large (now absent) planetary scale objects.

5. DISCUSSION OF COSMOGONIC IMPLICATIONS

Based on several lines of evidence (see Kavelaars et al. 2021, and reference therein), the cold population is primordial, meaning its H_r distribution has not evolved since the formation epoch. Given the shape similarity of the hot and cold populations in the range $H_r \simeq 5.5$ to 8.3, we hypothesize that the hot population has also preserved its primordial shape in that size range and the same physical mechanism was responsible for the accretion of bodies of that size in both the hot and cold forming regions. The physical conditions (*e.g.*, temperature, dynamical time scales) were likely very different in these two regions, and in particular the surface density in solids would likely have been orders of magnitude larger in the hot-forming region than at $\simeq 43$ au (Gomes et al. 2004; Nesvorný et al. 2020). If true, it follows that the formed planetesimal size distribution is at most a weak function of the local conditions, at least in the $H_r=5.5$ –8.3 range; over this range it is steeper than collisional equilibrium. Coupled with the match to the cold (believed to be primordial and unevolved) population, we thus conclude that at this size scale there was no appreciable collisional modification of the shape. This implies that the initial phase during which the hot population was in a dense collisional environment was of shorter duration than the collisional lifetime of $D \simeq 100$ km bodies. Benavidez et al. (2022) supports this picture, showing that the $D \gtrsim 100$ km size distribution’s shape does not change. They also conclude that long (100 Myr) instability phases do not produce successful matches to observational constraints.

330 Nesvorný et al. (2020) and Kavelaars et al. (2021) suggested that a candidate for this initial plan-
 331 etesimal forming phase is the Gravitational/Streaming Instability (GI/SI). The numerical simulations
 332 typically yield a size distribution that can be fit with an exponential cutoff functional form (Abod
 333 et al. 2019) that is also a good match to the cold population. Here we have shown that it is also a
 334 good match to the hot population with $D \lesssim 300$ km.

335 Our paradigm is that after planetesimal formation, the conditions in the hot-population formation
 336 region (in particular much higher surface density) permitted the creation of bigger objects, which
 337 thus erased the taper for $H_r < 5.5$. An important implication is that dwarf planets and larger objects
 338 then accumulated mass without altering the relative size distribution in the $H_r \simeq 6$ to 9 range (and
 339 possibly much smaller sizes). Two main mechanisms are usually invoked for this latter stage of
 340 accretion: runaway growth (reviewed by Lissauer 1993) and pebble accretion (*e.g.*, Ormel 2017).
 341 Runaway growth does not care about the size of objects it sweeps up, while in pebble accretion the
 342 very-big object mass accretion is from tiny pebbles. In this later case, our result implies that objects
 343 with sizes corresponding to $H_r = 5.5\text{--}8.3$ accumulate negligible further mass via pebbles.

344 If GI/SI is the planetesimal-formation mechanism, scalings indicate that the mass of the largest
 345 bodies formed is governed by the local solid surface density (to the third power) and heliocentric
 346 distance (to the 6th power) (Abod et al. 2019; Li et al. 2019). For a surface density varying with
 347 heliocentric distance to the -1.5 or -2 power between 25 and 45 au, this would not be a problem as the
 348 density drop would roughly compensate for the increase in distance. However, there are arguments
 349 that the surface density drops by a factor of ~ 1000 between these locations (*i.e.* Nesvorný et al.
 350 2020). It is thus surprising that two populations would have the same exponential cutoff shape.
 351 Some possible solutions to this dilemma are:

352 **(1)** the initial planetesimal formation process is actually only mildly sensitive to the density, but
 353 the creation of $H_r < 5$ bodies in the hot-population formation region proceeded efficiently, while in
 354 the cold belt these dynamics were not triggered due to the low surface density, or

355 **(2)** cold-population formation occurred in a localized over density (perhaps caused by a pressure
 356 bump) in an environment where the formed planetesimals are not confined to the overdense region,

357 while in contrast the hot population formed in an extended high-density zone where large-object
358 formation was possible through another process.

359 The first possibility is supported by [Klahr & Schreiber \(2020\)](#) who derive a criterion for the *min-*
360 *imum* object mass that can be created by GI/SI when accounting for diffusion due to turbulence.
361 Based on this criterion, they claim that the size distribution should be a Gaussian centered on this
362 minimum size ($D \simeq 80\text{--}85$ km with width ~ 45 km). Their minimum size is fairly insensitive to
363 heliocentric distance from 3 to 30 au, but then drops markedly at larger distances.

364 The second possibility would have to be the solution if GI/SI is the dominant mechanism, unless
365 the current theoretical scaling laws are incorrect. In these studies, there is a trigger density one
366 gets to and then GI/SI forms planetesimals quickly. This could result in the two regions having the
367 same shape because they both reached the same critical density, although the way they achieved that
368 density would have been different between the two populations.

369 Summarizing our discussion, we hypothesize that whatever mechanism created the first planetes-
370 imals up to ~ 400 km in diameter, it is largely insensitive to the global physical conditions, and
371 produces objects up to that size. In dense environments, some other process(es) takes over to build
372 bigger objects, without altering the size distribution from ~ 300 km down to a few 10s km or even
373 less.

374 **Acknowledgements:** We thank Wes Fraser for useful discussions while preparing this manuscript, and reviewer
 375 David Nesvorny for useful comments. This work was supported by the Programme National de Planétologie (PNP)
 376 of CNRS-INSU co-funded by CNES. BG acknowledges discovery grant funding support from NSERC. This research
 377 made use of the Canadian Advanced Network for Astronomy Research (CANFAR) and the facilities of the Canadian
 378 Astronomy Data Centre operated by the National Research Council of Canada with the support of the Canadian
 379 Space Agency. This research has made use of data and/or services provided by the International Astronomical Union’s
 380 Minor Planet Center. Based on observations obtained with MegaPrime/MegaCam, a joint project of CFHT and
 381 CEA/DAPNIA, at the Canada-France-Hawaii Telescope (CFHT) which is operated by the National Research Council
 382 (NRC) of Canada, the Institut National des Sciences de l’Univers of the Centre National de la Recherche Scientifique
 383 (CNRS) of France, and the University of Hawaii. The observations at the CFHT were performed with care and respect
 384 from the summit of Maunakea which is a significant cultural and historic site.

REFERENCES

- 385 Abedin, A. Y., Kavelaars, J. J., Greenstreet, S., 399 Bannister, M. T., Gladman, B. J., Kavelaars,
 386 et al. 2021, *AJ*, 161, 195, 400 J. J., et al. 2018, *ApJS*, 236, 18,
 387 doi: [10.3847/1538-3881/abe418](https://doi.org/10.3847/1538-3881/abe418) 401 doi: [10.3847/1538-4365/aab77a](https://doi.org/10.3847/1538-4365/aab77a)
- 388 Abod, C. P., Simon, J. B., Li, R., et al. 2019, *ApJ*, 402 Benavidez, P. G., Campo Bagatin, A., Curry, J.,
 389 883, 192, doi: [10.3847/1538-4357/ab40a3](https://doi.org/10.3847/1538-4357/ab40a3) 403 Álvarez-Candal, Á., & Vincent, J.-B. 2022,
 404 *MNRAS*, 514, 4876,
 390 Adams, E. R., Gulbis, A. A. S., Elliot, J. L., et al. 405 doi: [10.1093/mnras/stac1578](https://doi.org/10.1093/mnras/stac1578)
- 391 2014, *AJ*, 148, 55, 406 Bernstein, G. M., Trilling, D. E., Allen, R. L.,
 392 doi: [10.1088/0004-6256/148/3/55](https://doi.org/10.1088/0004-6256/148/3/55) 407 et al. 2004, *AJ*, 128, 1364, doi: [10.1086/422919](https://doi.org/10.1086/422919)
- 393 Alexandersen, M., Gladman, B., Kavelaars, J. J., 408 Brown, M. E. 2008, in *The Solar System Beyond*
 394 et al. 2016, *AJ*, 152, 111, 409 Neptune, ed. Barucci, M. A., Boehnhardt, H.,
 395 doi: [10.3847/0004-6256/152/5/111](https://doi.org/10.3847/0004-6256/152/5/111) 410 Cruikshank, D. P., & Morbidelli, A. , LPI
 411 (Tucson: University of Arizona Press), 335–344
- 396 Ashton, E., Gladman, B., Kavelaars, J. J., et al. 412 —. 2013, *ApJL*, 778, L34,
 397 2021, *Icarus*, 356, 113793, 413 doi: [10.1088/2041-8205/778/2/L34](https://doi.org/10.1088/2041-8205/778/2/L34)
 398 doi: [10.1016/j.icarus.2020.113793](https://doi.org/10.1016/j.icarus.2020.113793)

- 414 Di Ruscio, A., Fienga, A., Durante, D., et al.
415 2020, *A&A*, 640, A7,
416 doi: [10.1051/0004-6361/202037920](https://doi.org/10.1051/0004-6361/202037920)
- 417 Elliot, J. L., Kern, S. D., Clancy, K. B., et al.
418 2005, *AJ*, 129, 1117, doi: [10.1086/427395](https://doi.org/10.1086/427395)
- 419 Epanechnikov, V. A. 1969, *Theory of Probability*
420 & Its Applications, 14, 153,
421 doi: [10.1137/1114019](https://doi.org/10.1137/1114019)
- 422 Fraser, W. C., Batygin, K., Brown, M. E., &
423 Bouchez, A. 2013, *Icarus*, 222, 357,
424 doi: [10.1016/j.icarus.2012.11.004](https://doi.org/10.1016/j.icarus.2012.11.004)
- 425 Fraser, W. C., Brown, M. E., Morbidelli, A.,
426 Parker, A., & Batygin, K. 2014, *ApJ*, 782, 100,
427 doi: [10.1088/0004-637X/782/2/100](https://doi.org/10.1088/0004-637X/782/2/100)
- 428 Fraser, W. C., Kavelaars, J. J., Holman, M. J.,
429 et al. 2008, *Icarus*, 195, 827,
430 doi: [10.1016/j.icarus.2008.01.014](https://doi.org/10.1016/j.icarus.2008.01.014)
- 431 Gladman, B., Kavelaars, J. J., Petit, J.-M., et al.
432 2001, *AJ*, 122, 1051, doi: [10.1086/322080](https://doi.org/10.1086/322080)
- 433 Gladman, B., & Volk, K. 2021, *ARA&A*, 59, 203,
434 doi: [10.1146/annurev-astro-120920-010005](https://doi.org/10.1146/annurev-astro-120920-010005)
- 435 Gladman, B., Lawler, S. M., Petit, J.-M., et al.
436 2012, *AJ*, 144, 23,
437 doi: [10.1088/0004-6256/144/1/23](https://doi.org/10.1088/0004-6256/144/1/23)
- 438 Gomes, R. S., Morbidelli, A., & Levison, H. F.
439 2004, *Icarus*, 170, 492,
440 doi: [10.1016/j.icarus.2004.03.011](https://doi.org/10.1016/j.icarus.2004.03.011)
- 441 Greenstreet, S., Gladman, B., & McKinnon,
442 W. B. 2015, *Icarus*, 258, 267,
443 doi: [10.1016/j.icarus.2015.05.026](https://doi.org/10.1016/j.icarus.2015.05.026)
- 444 Greenstreet, S., Gladman, B., McKinnon, W. B.,
445 Kavelaars, J. J., & Singer, K. N. 2019, *ApJL*,
446 872, L5, doi: [10.3847/2041-8213/ab01db](https://doi.org/10.3847/2041-8213/ab01db)
- 447 Grundy, W. M., Noll, K. S., Buie, M. W., et al.
448 2019, *Icarus*, 334, 30,
449 doi: [10.1016/j.icarus.2018.12.037](https://doi.org/10.1016/j.icarus.2018.12.037)
- 450 Hendler, N. P., & Malhotra, R. 2020, *The*
451 *Planetary Science Journal*, 1, 75,
452 doi: [10.3847/PSJ/abbe25](https://doi.org/10.3847/PSJ/abbe25)
- 453 Hofgartner, J. D., Buratti, B. J., Benecchi, S. D.,
454 et al. 2021, *Icarus*, 356, 113723,
455 doi: [10.1016/j.icarus.2020.113723](https://doi.org/10.1016/j.icarus.2020.113723)
- 456 Huang, Y., Gladman, B., & Volk, K. 2022a, *ApJS*,
457 259, 54, doi: [10.3847/1538-4365/ac559a](https://doi.org/10.3847/1538-4365/ac559a)
- 458 —. 2022b, *VizieR Online Data Catalog*,
459 *J/ApJS/259/54*
- 460 Johansen, A., Oishi, J. S., Mac Low, M.-M., et al.
461 2007, *Nature*, 448, 1022,
462 doi: [10.1038/nature06086](https://doi.org/10.1038/nature06086)
- 463 Kavelaars, J., Jones, L., Gladman, B., Parker,
464 J. W., & Petit, J. 2008, in *The Solar System*
465 *Beyond Neptune*, ed. Barucci, M. A.,
466 Boehnhardt, H., Cruikshank, D. P., &
467 Morbidelli, A. , 59–69
- 468 Kavelaars, J. J., Petit, J.-M., Gladman, B., et al.
469 2021, *ApJL*, 920, L28,
470 doi: [10.3847/2041-8213/ac2c72](https://doi.org/10.3847/2041-8213/ac2c72)
- 471 Kavelaars, J. J., Jones, R. L., Gladman, B. J.,
472 et al. 2009, *AJ*, 137, 4917,
473 doi: [10.1088/0004-6256/137/6/4917](https://doi.org/10.1088/0004-6256/137/6/4917)
- 474 Kenyon, S. J. 2002, *PASP*, 114, 265,
475 doi: [10.1086/339188](https://doi.org/10.1086/339188)

- 476 Kenyon, S. J., Bromley, B. C., O'Brien, D. P., &
477 Davis, D. R. 2008, in *The Solar System Beyond*
478 Neptune, ed. M. A. Barucci, H. Boehnhardt,
479 D. P. Cruikshank, A. Morbidelli, & R. Dotson
480 (University of Arizona Press), 293
- 481 Klahr, H., & Schreiber, A. 2020, *ApJ*, 901, 54,
482 doi: [10.3847/1538-4357/abac58](https://doi.org/10.3847/1538-4357/abac58)
- 483 Kobayashi, H., Tanaka, H., & Okuzumi, S. 2016,
484 *ApJ*, 817, 105,
485 doi: [10.3847/0004-637X/817/2/105](https://doi.org/10.3847/0004-637X/817/2/105)
- 486 Lacerda, P., & Jewitt, D. C. 2007, *AJ*, 133, 1393,
487 doi: [10.1086/511772](https://doi.org/10.1086/511772)
- 488 Lacerda, P., Fornasier, S., Lellouch, E., et al.
489 2014, *ApJL*, 793, L2,
490 doi: [10.1088/2041-8205/793/1/L2](https://doi.org/10.1088/2041-8205/793/1/L2)
- 491 Lellouch, E., Santos-Sanz, P., Lacerda, P., et al.
492 2013, *A&A*, 557, A60,
493 doi: [10.1051/0004-6361/201322047](https://doi.org/10.1051/0004-6361/201322047)
- 494 Li, R., Youdin, A. N., & Simon, J. B. 2019, *ApJ*,
495 885, 69, doi: [10.3847/1538-4357/ab480d](https://doi.org/10.3847/1538-4357/ab480d)
- 496 Lissauer, J. J. 1993, *ARA&A*, 31, 129,
497 doi: [10.1146/annurev.aa.31.090193.001021](https://doi.org/10.1146/annurev.aa.31.090193.001021)
- 498 McKinnon, W. B., Richardson, D. C., Marohnic,
499 J. C., et al. 2020, *Science*, 367, aay6620,
500 doi: [10.1126/science.aay6620](https://doi.org/10.1126/science.aay6620)
- 501 Morbidelli, A., Bottke, W., Nesvorný, D., &
502 Levison, H. 2009, *Icarus*, 204, 558
- 503 Morbidelli, A., Levison, H. F., Tsiganis, K., &
504 Gomes, R. 2005, *Nature*, 435, 462,
505 doi: [10.1038/nature03540](https://doi.org/10.1038/nature03540)
- 506 Morbidelli, A., & Nesvorný, D. 2020, in *The*
507 *Trans-Neptunian Solar System*, ed. D. Prialnik,
508 M. A. Barucci, & L. Young (Elsevier US),
509 25–59,
510 doi: [10.1016/B978-0-12-816490-7.00002-3](https://doi.org/10.1016/B978-0-12-816490-7.00002-3)
- 511 Morbidelli, A., Nesvorný, D., Bottke, W. F., &
512 Marchi, S. 2021, *Icarus*, 356, 114256,
513 doi: [10.1016/j.icarus.2020.114256](https://doi.org/10.1016/j.icarus.2020.114256)
- 514 Nesvorný, D. 2018, *ARA&A*, 56, 137,
515 doi: [10.1146/annurev-astro-081817-052028](https://doi.org/10.1146/annurev-astro-081817-052028)
- 516 Nesvorný, D., & Vokrouhlický, D. 2016, *ApJ*, 825,
517 94, doi: [10.3847/0004-637X/825/2/94](https://doi.org/10.3847/0004-637X/825/2/94)
- 518 Nesvorný, D., Vokrouhlický, D., & Roig, F. 2016,
519 *ApJL*, 827, L35,
520 doi: [10.3847/2041-8205/827/2/L35](https://doi.org/10.3847/2041-8205/827/2/L35)
- 521 Nesvorný, D., Vokrouhlický, D., Alexandersen,
522 M., et al. 2020, *AJ*, 160, 46,
523 doi: [10.3847/1538-3881/ab98fb](https://doi.org/10.3847/1538-3881/ab98fb)
- 524 Ormel, C. W. 2017, in *Astrophysics and Space*
525 *Science Library*, Vol. 445, Formation, Evolution,
526 and Dynamics of Young Solar Systems, ed.
527 M. Pessah & O. Gressel, 197,
528 doi: [10.1007/978-3-319-60609-5_7](https://doi.org/10.1007/978-3-319-60609-5_7)
- 529 Parker, A., Buie, M. W., Grundy, W., et al. 2018,
530 in *AAS/Division for Planetary Sciences Meeting*
531 *Abstracts*, Vol. 50, AAS/Division for Planetary
532 Sciences Meeting Abstracts #50, 509.02
- 533 Parker, A. H., & Kavelaars, J. J. 2010, *ApJL*, 722,
534 L204, doi: [10.1088/2041-8205/722/2/L204](https://doi.org/10.1088/2041-8205/722/2/L204)
- 535 Parzen, E. 1962, *Ann. Math. Statist.*, 33, 1065,
536 doi: [10.1214/aoms/1177704472](https://doi.org/10.1214/aoms/1177704472)

- 537 Pedregosa, F., Varoquaux, G., Gramfort, A., et al. 569 Shannon, A., Wu, Y., & Lithwick, Y. 2016, *ApJ*,
538 2011, *Journal of Machine Learning Research*, 570 818, 175, doi: [10.3847/0004-637X/818/2/175](https://doi.org/10.3847/0004-637X/818/2/175)
539 12, 2825 571 Sheppard, S. S., Udalski, A., Trujillo, C., et al.
540 Petit, J., Kavelaars, J. J., Gladman, B., & Lored, 572 2011, *AJ*, 142, 98,
541 T. 2008, in *The Solar System Beyond Neptune*, 573 doi: [10.1088/0004-6256/142/4/98](https://doi.org/10.1088/0004-6256/142/4/98)
542 ed. Barucci, M. A., Boehnhardt, H., 574 Singer, K. N., McKinnon, W. B., Gladman, B.,
543 Cruikshank, D. P., & Morbidelli, A. , 71–87 575 et al. 2019, *Science*, 363, 955,
544 Petit, J., & Mousis, O. 2004, *Icarus*, 168, 409, 576 doi: [10.1126/science.aap8628](https://doi.org/10.1126/science.aap8628)
545 doi: [10.1016/j.icarus.2003.12.013](https://doi.org/10.1016/j.icarus.2003.12.013) 577 Souami, D., Braga-Ribas, F., Sicardy, B., et al.
546 Petit, J.-M., Kavelaars, J. J., Gladman, B. J., 578 2020, *A&A*, 643, A125,
547 et al. 2011, *AJ*, 142, 131, 579 doi: [10.1051/0004-6361/202038526](https://doi.org/10.1051/0004-6361/202038526)
548 doi: [10.1088/0004-6256/142/4/131](https://doi.org/10.1088/0004-6256/142/4/131) 580 Spencer, J. R., Stern, S. A., Moore, J. M., et al.
549 —. 2017, *AJ*, 153, 236, 581 2020, *Science*, 367, aay3999,
550 doi: [10.3847/1538-3881/aa6aa5](https://doi.org/10.3847/1538-3881/aa6aa5) 582 doi: [10.1126/science.aay3999](https://doi.org/10.1126/science.aay3999)
551 Pike, R. E., Fraser, W. C., Schwamb, M. E., et al. 583 Stansberry, J., Grundy, W., Brown, M., et al.
552 2017, *AJ*, 154, 101, 584 2008, in *The Solar System Beyond Neptune*, ed.
553 doi: [10.3847/1538-3881/aa83b1](https://doi.org/10.3847/1538-3881/aa83b1) 585 M. A. Barucci, H. Boehnhardt, D. P.
554 Pitjeva, E. V., & Pitjev, N. P. 2018, *Celestial* 586 Cruikshank, A. Morbidelli, & R. Dotson
555 *Mechanics and Dynamical Astronomy*, 130, 57, 587 (University of Arizona Press), 161
556 doi: [10.1007/s10569-018-9853-5](https://doi.org/10.1007/s10569-018-9853-5) 588 Tancredi, G., & Favre, S. 2008, *Icarus*, 195, 851,
557 Rosenblatt, M. 1956, *Ann. Math. Statist.*, 27, 832, 589 doi: [10.1016/j.icarus.2007.12.020](https://doi.org/10.1016/j.icarus.2007.12.020)
558 doi: [10.1214/aoms/1177728190](https://doi.org/10.1214/aoms/1177728190) 590 Tegler, S. C., Romanishin, W., & Consolmagno,
559 Schäfer, U., Yang, C.-C., & Johansen, A. 2017, 591 G. J. 2003, *ApJL*, 599, L49, doi: [10.1086/381076](https://doi.org/10.1086/381076)
560 *A&A*, 597, A69, 592 Vachier, F., Berthier, J., & Marchis, F. 2012,
561 doi: [10.1051/0004-6361/201629561](https://doi.org/10.1051/0004-6361/201629561) 593 *A&A*, 543, A68,
562 Schaller, E. L., & Brown, M. E. 2007, *ApJL*, 659, 594 doi: [10.1051/0004-6361/201118408](https://doi.org/10.1051/0004-6361/201118408)
563 L61, doi: [10.1086/516709](https://doi.org/10.1086/516709) 595 Van Laerhoven, C., Gladman, B., Volk, K., et al.
564 Schlichting, H. E., & Sari, R. 2011, *ApJ*, 728, 68, 596 2019, *AJ*, 158, 49,
565 doi: [10.1088/0004-637X/728/1/68](https://doi.org/10.1088/0004-637X/728/1/68) 597 doi: [10.3847/1538-3881/ab24e1](https://doi.org/10.3847/1538-3881/ab24e1)
566 Schwamb, M. E., Fraser, W. C., Bannister, M. T., 598 Vilenius, E., Kiss, C., Müller, T., et al. 2014,
567 et al. 2019, *ApJS*, 243, 12, 599 *A&A*, 564, A35,
568 doi: [10.3847/1538-4365/ab2194](https://doi.org/10.3847/1538-4365/ab2194) 600 doi: [10.1051/0004-6361/201322416](https://doi.org/10.1051/0004-6361/201322416)

601 Weryk, R. J., Lilly, E., Chastel, S., et al. 2016,
602 arXiv e-prints, arXiv:1607.04895.
603 <https://arxiv.org/abs/1607.04895>

604 Willmer, C. N. A. 2008.
605 <http://mips.as.arizona.edu/~cnaw/sun.html>

APPENDIX

A. KERNEL DENSITY ESTIMATOR (KDE)

To avoid the shortcomings of classical histograms due to size and location of the bins, we use a Kernel Density Estimator (KDE) (Rosenblatt 1956; Parzen 1962) to estimate the true H_r distribution (see https://en.wikipedia.org/wiki/Kernel_density_estimation for an easy and basic introduction to KDEs). The kernel is a non-negative function that smoothes the contribution of each datum over an interval which size is determined by the *bandwidth* parameter. There exists a variety of kernels; we use an Epanechnikov finite extent kernel (Epanechnikov 1969), as it is optimal in a mean square error sense.

The bandwidth is an important parameter that we determine using the empirical approach of cross-validation. This empirical approach to model parameter selection does not depend on (dubious) assumptions about the underlying data's distribution and thus is very flexible. For the cold OSSOS++ sample the optimal bandwidth is 0.4, which we use to plot Fig. 1. For the hot sample, the optimal bandwidth depends rather strongly on the inclusion or exclusion of the few objects at the tails of the distribution, especially at the bright end where the H_r spread is very uneven. This means that the best bandwidth is very different at the large size and the small size ends of the range, so we renormalize the H_r values to make them more uniform ($Y_r = 10^{0.1(H_r-9)}$) and then use an optimal bandwidth of 0.1 in this new variable.

In our computations, we use the implementation from the scikit-learn python package (Pedregosa et al. 2011). We then scale the KDE to the total number of objects in each component of the main classical Kuiper Belt per magnitude and show the result in Fig. 1.

B. MASS OF THE BELT

We first derive the relation between H_r and the TNO mass M . The apparent magnitude m_r in a given filter band (CFHTLS- r' here) is related to its radius r , in km, its geometric albedo ν_r , its distance to the Sun R and to the observer on Earth Δ (both in au), its phase angle γ , the phase

631 function $\Phi(\gamma)$, the rotational lightcurve function $f(t)$ and the magnitude of the Sun $m_{r,Sun}$ in the
 632 same band, by

$$633 \quad m_r = m_{r,Sun} - 2.5 \log_{10} \left(\nu_r \left(\frac{r}{1 \text{ km}} \right)^2 \Phi(\gamma) f(t) \right) + 2.5 \log_{10} \left(2.25 \times 10^{16} \frac{R^2 \Delta^2}{\text{au}^4} \right) \quad (\text{B1})$$

634 Here we assume $f(t) = 1$ as the average of a rapid periodic function. From H_r definition, we have

$$635 \quad H_r = m_r + 2.5 \log_{10}(\Phi(\gamma)) - 2.5 \log_{10} \left(\frac{R^2 \Delta^2}{\text{au}^4} \right)$$

$$636 \quad = m_{r,Sun} + 2.5 \log_{10} (2.25 \times 10^{16}) - 2.5 \log_{10} \left(\nu_r \left(\frac{r}{1 \text{ km}} \right)^2 \right)$$

637 For the cfhtls-r filter, $m_{r,Sun} = -26.94$ in the AB system (Willmer 2008) and therefore

$$638 \quad H_r = 13.94 - 2.5 \log_{10} \left(\nu_r \left(\frac{r}{1 \text{ km}} \right)^2 \right) \quad (\text{B2})$$

639 Denoting bulk density as ρ , their mass $M = \frac{4\pi}{3} \rho r^3$ can be written, using Eq. B2, as

$$640 \quad M = \frac{4\pi}{3} \frac{\rho}{\nu_r^{3/2}} 10^{(13.94 - H_r) \frac{3}{5}} = B \frac{\rho}{\nu_r^{3/2}} 10^{-\frac{3H_r}{5}} \quad (\text{B3})$$

641 with $B = \frac{4\pi}{3} 10^{13.96 \frac{3}{5}} \text{ kg} = 9.685 \times 10^8 \text{ kg}$, and ρ given in kg.km^{-3} ($1 \text{ g.cm}^{-3} = 10^{12} \text{ kg.km}^{-3}$).

642 The computation of TNO mass from its absolute magnitude H_r thus strongly depends on the two
 643 unknowns ρ and ν_r . Conservatively assuming that ρ can vary from 0.5 g.cm^{-3} to 2 g.cm^{-3} , and ν_r
 644 from 0.06 (as seen from the comets), to 0.24 (Arrokoth), we can formally have a variation by a factor
 645 of ~ 30 in the mass of individual objects.

646 B.1. *The hot belt*

647 For a scenario of fixed values of the albedo and the bulk density, the mass of the hot belt is
 648 dominated by the few largest bodies (such as Makemake, Quaoar, Varda or Varuna) but the predicted
 649 mass of these large bodies is badly overestimated if using nominal values of these quantities. With
 650 the nominal values of $\nu_r = 0.08$ (Lacerda et al. 2014), $\rho = 1 \text{ g/cm}^3$ (Gladman et al. 2001; Fraser et al.
 651 2014) and $H_r = -0.31$, one would find a mass for Makemake of $1.1 \cdot 10^{-2} M_{\oplus}$ when its actual mass is
 652 $5.2 \cdot 10^{-4} M_{\oplus}$ (Parker et al. 2018). The discrepancy decreases with increasing H_r but is still of a factor
 653 of 2 for Varuna at $H_r = 3.59$.

The simple solution of this issues is that [Stansberry et al. \(2008\)](#) showed a correlation between object size and geometric albedo, which [Fraser et al. \(2008\)](#) modelled as $\nu \propto r^\beta$. It is also likely that the density of a body increases with its size due to self-compression. In the mass-to- H_r relation, the important factor is $\rho\nu^{-3/2}$ which we then model as $\rho\nu^{-3/2} = A(M/1 \text{ kg})^\gamma$. We select $\gamma = 0.77$ with resulting $A \sim 6.7 \times 10^{28}$ for ρ expressed in kg.km^{-3} to roughly match the known masses of Makemake, Quaoar ($M \simeq 1.4 \cdot 10^{21}\text{kg}$, [Vachier et al. \(2012\)](#); [Fraser et al. \(2013\)](#)), Varda ($M \simeq 2.45 \cdot 10^{20}\text{kg}$, [Souami et al. \(2020\)](#)), Varuna ($1.5 \cdot 10^{20}\text{kg}$, [Lacerda & Jewitt \(2007\)](#); [Lellouch et al. \(2013\)](#)) and (55637) 2002 UX25 ($1.2 \cdot 10^{20}\text{kg}$, [Brown \(2013\)](#)). We use this dependency for the large bodies until the $\rho\nu^{-3/2}$ factor reaches its nominal value for $\rho = 1\text{g/cm}^3$ and $\nu_r = 0.08$, which occurs at $M = 5.6 \cdot 10^{19}\text{kg}$ and $H_r = 4.82$. For smaller masses (larger H_r), we use the nominal values for ρ and ν .

Brightward of $H_r = 5.47$, we use the raw MPC absolute magnitude distribution. Between $H_r = 5.47$ and $H_r = 8.3$ we use the debiased H_r distributions shown in [Fig. 1](#). Faintward of this limit, we use the exponential cutoff from the cold belt ([eq. B4](#)) scaled-up by a factor of 2.2 as in [Figure 2](#). As expected the mass is not concentrated at any given size. The total mass of the hot main classical belt is $0.012 M_\oplus$.

B.2. The cold belt

For the cold population, all TNOs are small enough to be in the regime where albedos and densities that are not correlated with their size. We use the nominal $\rho = 1000\text{kg/m}^3$ with more reflective $\nu_r = 0.15$ ([Fraser et al. 2014](#); [Lacerda et al. 2014](#)) estimated for cold objects. The debiased mass of the cold belt, brighter than $H_r = 8.3$ comes out as $0.0010 M_\oplus$.

For cold TNOs with $H_r > 8.3$, we use the exponential cutoff parameterization from [Kavelaars et al. \(2021\)](#),

$$N(< H_r) = 10^{\alpha(H_r - H_o)} \exp[-10^{-\beta(H_r - H_B)}] \quad (\text{B4})$$

where N is the total population for TNOs with absolute magnitude less than H_r ; $H_o = -2.6$ is a normalization factor, $\alpha = 0.4$ is the asymptotic logarithmic slope at large H_r , $\beta = 0.25$ is the strength of the exponential tapering and $H_B = 8.1$ is the H_r value at which the exponential taper begins to

680 dominate as one moves towards brighter magnitudes⁹. We caution that there is degeneracy in this
681 parameterization, which allows individual parameters to have large variations as long as the others
682 change in a correlated way, which results in the cumulative population curve being very similar. This
683 yields a mass of $0.0011 M_{\oplus}$ for cold $H_r > 8.3$ TNOs, assuming $\alpha = 0.4$ continues.

684 Thus the total mass of the cold belt is $0.0021 M_{\oplus}$, for the assumed albedo and bulk density, or
685 about 1/6 of our hot-belt mass estimate.

⁹ Note that numbers in Table 1 are obtained from debiasing of OSSOS data, not from this formula.